

Corrected: Publisher Correction

# Migrasome formation is mediated by assembly of micron-scale tetraspanin macrodomains

Yuwei Huang<sup>1,2,6</sup>, Ben Zucker<sup>3,6</sup>, Shaojin Zhang<sup>1,2,6</sup>, Sharon Elias<sup>3</sup>, Yun Zhu<sup>4</sup>, Hui Chen<sup>5</sup>, Tianlun Ding<sup>1,2</sup>, Ying Li<sup>1,2</sup>, Yujie Sun<sup>4</sup>, Jizhong Lou<sup>5</sup>, Michael M. Kozlov<sup>ID 3\*</sup> and Li Yu<sup>ID 1,2\*</sup>

**Migrasomes are recently discovered cellular organelles that form as large vesicle-like structures on retraction fibres of migrating cells. While the process of migrasome formation has been described before, the molecular mechanism underlying migrasome biogenesis remains unclear. Here, we propose that the mechanism of migrasome formation consists of the assembly of tetraspanin- and cholesterol-enriched membrane microdomains into micron-scale macrodomains, which swell into migrasomes. The major finding underlying the mechanism is that tetraspanins and cholesterol are necessary and sufficient for migrasome formation. We demonstrate the necessity of tetraspanins and cholesterol via live-cell experiments, and their sufficiency by generating migrasome-like structures in reconstituted membrane systems. We substantiate the mechanism by a theoretical model proposing that the key factor driving migrasome formation is the elevated membrane stiffness of the tetraspanin- and cholesterol-enriched macrodomains. Finally, the theoretical model was quantitatively validated by experimental demonstration of the membrane-stiffening effect of tetraspanin 4 and cholesterol.**

Migrasomes are recently discovered cellular organelles whose formation is closely associated with cell migration. When cells crawl on extracellular substrates, long membrane projections, referred to as retraction fibres (RFs), are pulled out of the plasma membrane at the rear of the cell<sup>1</sup>. The RFs serve as tethers stretched between the cell body and the substrate<sup>2</sup>. Migrasomes are large vesicle-like structures that start to grow on the RFs hours after the initiation of RF formation<sup>3</sup>. Eventually, as the cell migrates away, the connections between the cell and the RFs break, the RFs disintegrate and the migrasomes detach from the cell. During zebrafish gastrulation, migrasomes release developmental cues, including CXCL12, into defined locations in embryos to modulate organ morphogenesis<sup>4</sup>. Thus, migrasomes have been proposed to provide a mechanism for integrating and relaying spatiotemporal chemical information for cell–cell communication<sup>4</sup>. So far, the molecular mechanism underlying migrasome formation has never been addressed.

Tetraspanin 4 (TSPAN4) was previously shown to be abundant in the migrasome membrane<sup>2</sup>. Proteins of the tetraspanin family, which has 33 members, are present in every cell type, and all of them contain four transmembrane domains<sup>5</sup>. Tetraspanins can laterally segregate in the membrane plane into tetraspanin-enriched microdomains (TEMs)<sup>6</sup>, which are around 100 nm in size, and contain, in addition to tetraspanins, a high concentration of cholesterol and a set of tetraspanin-associated proteins<sup>7,8</sup>.

## Results

**TSPAN4 is necessary for migrasome formation.** We found that overexpression of 14 out of the 33 known mammalian tetraspanins enhanced migrasome formation (Fig. 1a). Among these 14 tetraspanins, 9 had a strong effect (Fig. 1a). Since TSPAN4 is one of most effective tetraspanins for migrasome induction, we chose it for in-depth study.

To study whether the TSPAN4 expression level can affect migrasome formation, we established three normal rat kidney (NRK) epithelial cell lines that stably express different levels of TSPAN4 and green fluorescent protein (GFP) (Fig. 1b,d; Supplementary Fig. 1a). We found that overexpression of TSPAN4 enhanced migrasome formation in a dose-dependent manner (Fig. 1b,c). It is worth noting that TSPAN4-GFP appears as a smeared double band on western blots, which is a result of glycosylation (Supplementary Fig. 1b). Among the nine tetraspanins that can significantly induce migrasome formation, TSPAN4 was the most highly expressed in human gastric carcinoma MGC-803 cells (Supplementary Fig. 1c) and NRK cells (Supplementary Table 1).

To test whether TSPAN4 is required for migrasome formation, we generated *TSPAN4* knockout cell lines using the clustered regularly interspaced short palindromic repeats (CRISPR)–Cas9 technique. Knockout of *TSPAN4* did indeed impair migrasome formation in MGC-803 cells (Fig. 1e–g) and NRK cells (Supplementary Fig. 1d,e).

Altogether, these data suggest that tetraspanins are necessary for migrasome formation. It is worth noting that in L929 cells (NCTC clone 929 of strain L, mouse connective tissue), knocking out *Tspan4* did not impair migrasome formation, presumably due to the presence of other migrasome-forming tetraspanins (Supplementary Fig. 1f).

**Dynamics of TSPAN4 recruitment to migrasomes during migrasome formation.** Next, we studied the dynamics of TSPAN4 repartitioning on RF membranes during the course of migrasome biogenesis. First, we measured the mean fluorescence intensity of TSPAN4-GFP on migrasomes and RFs. We found that during the rapid initial phase of migrasome growth, the mean intensity of TSPAN4-GFP rose on migrasomes, while it slightly decreased on

<sup>1</sup>The State Key Laboratory of Membrane Biology, Tsinghua University–Peking University Joint Center for Life Sciences, School of Life Sciences, Tsinghua University, Beijing, China. <sup>2</sup>Beijing Frontier Research Center for Biological Structure, Beijing, China. <sup>3</sup>Department of Physiology and Pharmacology, Sackler Faculty of Medicine, Tel Aviv University, Tel Aviv, Israel. <sup>4</sup>The State Key Laboratory of Membrane Biology, Biodynamic Optical Imaging Center (BIOPIC), School of Life Sciences, Peking University, Beijing, China. <sup>5</sup>Key Laboratory of RNA Biology, Institute of Biophysics, Chinese Academy of Sciences, Beijing, China. <sup>6</sup>These authors contributed equally: Yuwei Huang, Ben Zucker, Shaojin Zhang. \*e-mail: [michk@tauex.tau.ac.il](mailto:michk@tauex.tau.ac.il); [liyulab@mail.tsinghua.edu.cn](mailto:liyulab@mail.tsinghua.edu.cn)

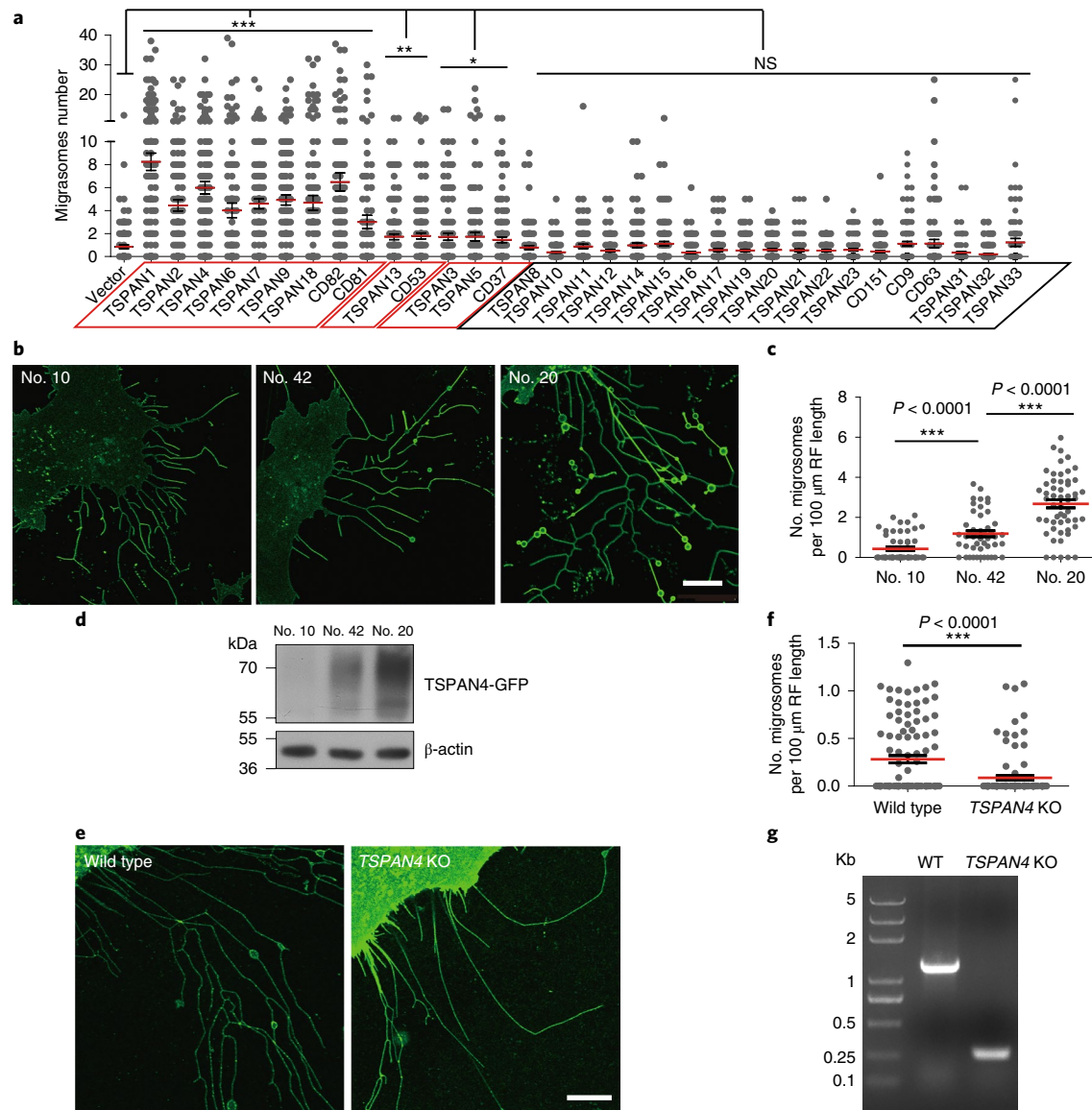


**Fig. 1 | TSPAN4 is necessary for migrasome formation.** **a**, All 33 members of the tetraspanin family were analysed for their ability to induce migrasome formation following overexpression in NRK cells. Migrasome numbers were quantified based on fluorescent images taken by confocal microscopy. The experiment was done once. Data shown represent the mean  $\pm$  s.e.m.;  $n \geq 100$  cells. \* $P < 0.05$ , \*\* $P < 0.01$ , \*\*\* $P < 0.001$ . Red outlines, groups showed significant difference; black outlines, groups showed no significant difference. Exact sample sizes and  $P$  values are presented in Supplementary Table 4. **b**, NRK cells (cell numbers 10, 42 and 20) stably expressing different levels of TSPAN4-GFP were analysed for the number of migrasomes by confocal microscopy. Scale bar, 10  $\mu\text{m}$ . **c**, The number of migrasomes per 100  $\mu\text{m}$  of RF from images like those shown in **b** was quantified. Data shown represent the mean  $\pm$  s.e.m.;  $n = 54$  (no. 10), 47 (no. 42) and 54 (no. 20) cells, each pooled from 3 independent experiments. **d**, The TSPAN4-GFP expression level of cell lines from **b** was analysed by western blotting. **e**, A TSPAN4 knockout (KO) MGC-803 cell line was established using the CRISPR-Cas9 technique. Wild-type (WT) and TSPAN4 KO cells were analysed by confocal microscopy for the number of migrasomes. Scale bar, 10  $\mu\text{m}$ . **f**, Cells from WT and TSPAN4 KO MGC-803 cells were quantified for the migrasome number per 100  $\mu\text{m}$  of RFs. Data shown represent the mean  $\pm$  s.e.m.;  $n = 100$  cells for each genotype, each pooled from 3 independent experiments. **g**, Verification of the MGC-803 TSPAN4 KO cell line by PCR. The unprocessed blots images related to **d** are presented in Supplementary Fig. 6. Experiments related to **b-g** were independently repeated three times. Two-tailed unpaired  $t$ -tests were used for statistical analyses. The statistical details for **a, c** and **f** are available in Supplementary Table 4.

RFs (Fig. 2a,b). After the migrasomes reached their maximal size, the mean intensity of migrasomal TSPAN4-GFP remained constant (Fig. 2a,b). The migrasomal state characterized by a constant size and TSPAN4 intensity will be referred to as the steady phase.

To substantiate this observation, we carried out fluorescence recovery after photobleaching (FRAP) assays on migrasomes during the growth and steady phases. We observed a fast recovery of the migrasomal TSPAN4 signal in the growth phase (Fig. 2c; Supplementary Fig. 2a-c), whereas in the steady phase, the TSPAN4

signal did not recover at all (Fig. 2c; Supplementary Fig. 2a-c). These results further support the conclusion that TSPAN4 is recruited to migrasomes during the growth phase. The recruitment of TSPAN4 stops after a migrasome enters the steady phase.

The recovery of bleached TSPAN4-GFP in migrasomes during the growth phase indicates that TSPAN4-GFP can be recruited from RFs to migrasomes. Next, we tested whether TSPAN4-GFP can also move in the opposite direction; that is, from a migrasome to the RF membrane. For this purpose, we bleached the TSPAN4-GFP

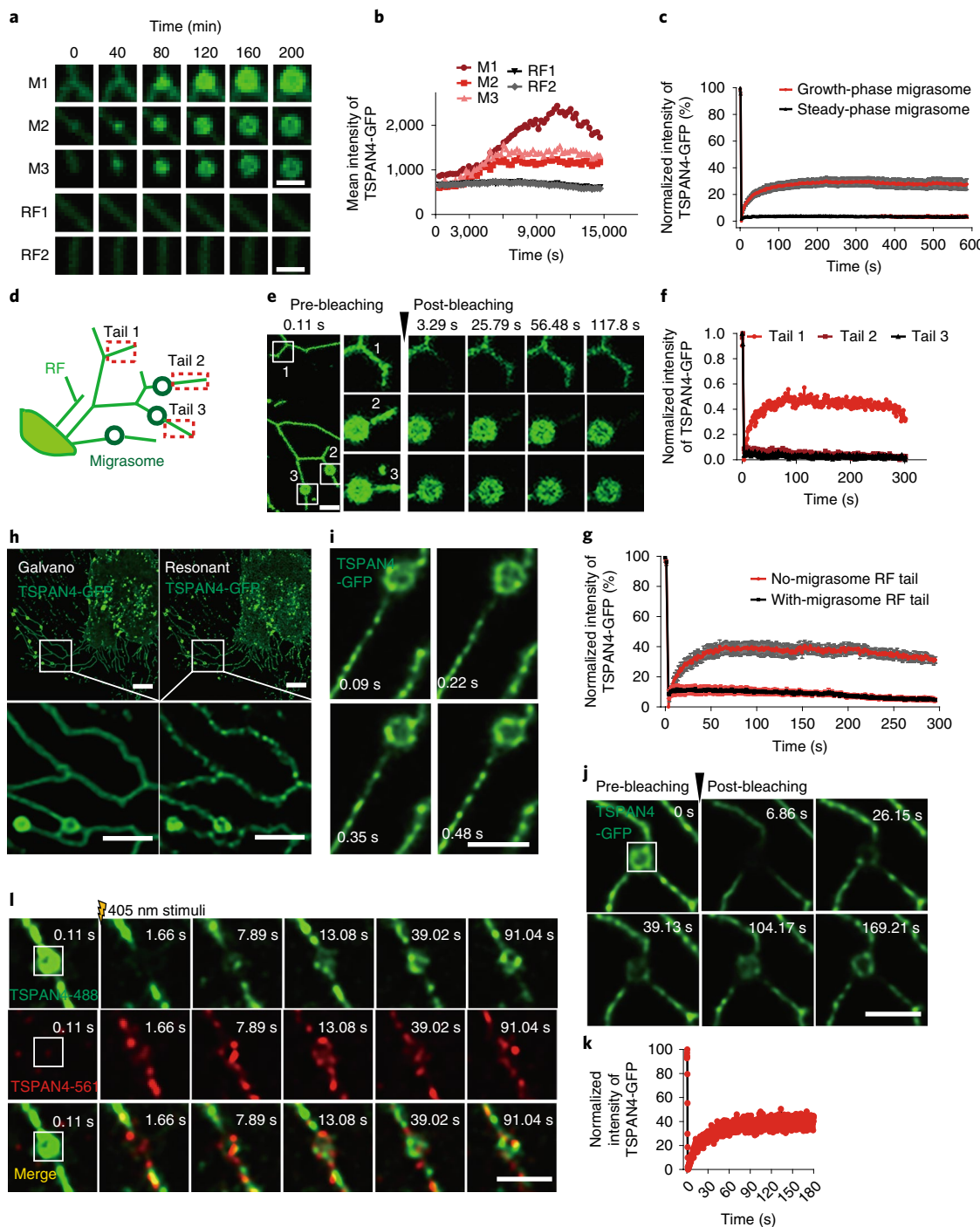


**Fig. 2 | Dynamics of TSPAN4 recruitment to migrasomes during migrasome formation.** **a**, Time-lapse imaging of migrasome (M) formation. Green signal, TSPAN4-GFP. Scale bar, 2 μm. **b**, Three migrasomes and two sections of RFs in **a** were analysed for the change of mean TSPAN4-GFP fluorescence intensity during migrasome formation. **c**, Normalized intensity of TSPAN4-GFP on growth-phase and steady-phase migrasomes was analysed during FRAP assays.  $n=37$  for growth-phase migrasomes,  $n=39$  for steady-phase migrasomes; data from 26 independent experiments, mean  $\pm$  s.e.m. **d**, Working model of FRAP analysis of RFs. RF tail 1 is directly connected to the cell body, tails 2 and 3 are separated from the cell body by migrasomes. **e**, Time-lapse images showing FRAP analysis of RFs in TSPAN4-GFP-expressing NRK cells. Tails 1, 2 and 3 are localized as shown in the working model in **d**. Scale bar, 2 μm. **f**, Normalized mean fluorescence intensity of TSPAN4-GFP on RFs in **e**. **g**, Normalized intensity of TSPAN4-GFP on no-migrasome RF tails and with-migrasome RF tails (like RF tails 1, 2 and 3 in **d**).  $n=13$  for no-migrasome RF tails,  $n=18$  for with-migrasome RF tails; data from 15 independent experiments, mean  $\pm$  s.e.m. **h**, TSPAN4-GFP-expressing NRK cells were imaged by galvanometer scanning mode (1 frame s<sup>-1</sup>) and resonant scanning mode (30 frames s<sup>-1</sup>). Scale bars, 10 μm, 5 μm (zoomed-in images). **i**, Time-lapse images of a migrasome and RF on a TSPAN4-GFP-expressing cell obtained by resonant scanning mode. Scale bar, 5 μm. **j**, Time-lapse images of a migrasome using the resonant scanning mode. Scale bar, 2.5 μm. **k**, Time course of the normalized mean fluorescence intensity of TSPAN4-GFP in migrasomes analysed by FRAP as in **j**. **l**, Time-lapse images of a migrasome taken by resonant scanning mode using TSPAN4-mMaple3 photoconverted from green to red by 405 nm laser irradiation. Scale bar, 2.5 μm. Experiments were independently repeated 9 times (**a** and **b**), 26 times (**c**), 15 times (**e**–**g**), 3 times (**h**), 7 times (**i**); 12 times (**j** and **k**), or 10 times (**l**). The statistical details for **c** and **g** are available in Supplementary Table 4.

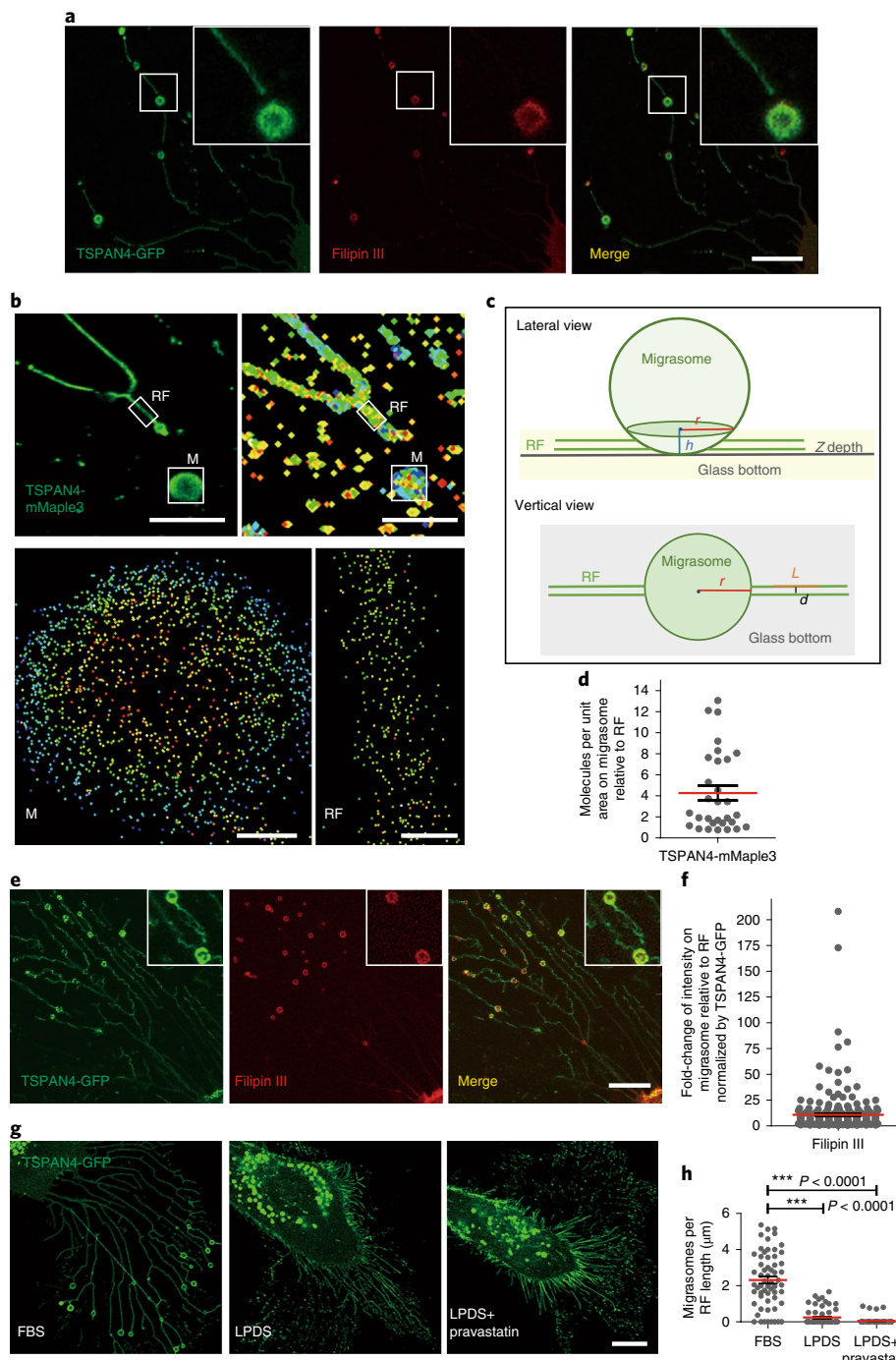


**Fig. 3 | The migrasomal membrane is a TEMA.** **a**, TSPAN4-expressing NRK cells were stained using filipin III. Scale bar, 10  $\mu\text{m}$ . **b**, Single-molecule counting by PALM. Upper left: PALM image of a migrasome and RF from NRK TSPAN4-mMaple3 cells. Upper right: the location of single TSPAN4-mMaple3 molecules; colour from red to blue indicates the z-positions from bottom to top. Lower panels, the enlarged ROIs in the upper images. Scale bars, 2.5  $\mu\text{m}$  (upper panels), 200 nm (lower left), 100 nm (lower right). **c**, Schematic diagram for calculating the surface area in the bottom 200-nm segment of RFs and migrasomes. **d**, The average number of TSPAN4-mMaple3 molecules per unit area from **b** was quantified. The migrasome and the connected RF were set as a pair, and the fold-enrichment of TSPAN4-mMaple3 molecules on the migrasome was calculated. Data shown represent the mean  $\pm$  s.e.m. ( $4.269 \pm 0.697$ ),  $n = 30$  pairs. **e**, Z-projection of z-stack images of TSPAN4-GFP-expressing NRK cells that were stained using filipin III. Scale bar, 10  $\mu\text{m}$ . **f**, Cholesterol levels on migrasomes relative to RFs. Based on images in **e**, the following parameters were determined: filipin III intensity on migrasome,  $I_{\text{pM}}$ ; TSPAN4-GFP intensity on migrasome,  $I_{\text{tM}}$ ; filipin III intensity on RF,  $I_{\text{pR}}$ ; TSPAN4-GFP intensity on RF,  $I_{\text{tR}}$ . Within a pair, the values of  $I_{\text{pM}}/I_{\text{pR}}$  and  $I_{\text{tM}}/I_{\text{tR}}$  were calculated. The fold-change values,  $(I_{\text{pM}}/I_{\text{pR}})/(I_{\text{tM}}/I_{\text{tR}})$ , is displayed. Data shown represent the mean  $\pm$  s.e.m. ( $10.79 \pm 1.267$ ),  $n = 255$  pairs. **g**, TSPAN4-GFP expressing cells were pretreated with 10% full cholesterol medium (FBS), LPDS and cholesterol-depletion medium with 30  $\mu\text{M}$  pravastatin. Scale bar, 10  $\mu\text{m}$ . **h**, Statistics of the migrasome numbers per 100  $\mu\text{m}$  RF length under the same conditions as for **g**. Data shown represent the mean  $\pm$  s.e.m.; each group had  $n = 60$  cells. Experiments were performed 3 (**a** and **e–h**) or 9 times (**b** and **d**). Quantifications in **d**, **f** and **h** are pooled from 9 (**d**) or 3 (**f** and **h**) independent experiments with statistical details provided in Supplementary Table 4. For **a**, images are representative of 18 cells. Two-tailed unpaired t-tests were used for statistical analyses.

fluorescence along a section of the RF between the migrasome and the RF tip (Fig. 2d, tail 2, 3). As a control, we used the fluorescence recovery of a section of the RF that was directly connected to the cell body (Fig. 2d, tail 1). In the latter case we found that the TSPAN4 signal recovered quickly after bleaching. In contrast, in the RF region connected to the distal side of the migrasome, the TSPAN4 signal did not recover after bleaching (Fig. 2e–g). Thus, TSPAN4 does not move from the migrasome to the RF. Taken together, these data suggest that TSPAN4 is recruited to the migrasomes from the RFs during the migrasomal growth phase, and TSPAN4 cannot move out once it is recruited to the migrasome.

**TSPAN4 forms discrete fast-moving puncta that concentrate on the migrasomal surface.** To study the organization of TSPAN4 on the RF and migrasomal membranes, we imaged cells in the resonant scanning mode, which gives much faster imaging speed ( $30\text{ frames s}^{-1}$ ) than the regularly used galvanometer scanning mode ( $1\text{ frame s}^{-1}$ ). Strikingly, we found that TSPAN4-GFP on both the RF and the migrasome appeared as fast-moving, discrete puncta (Fig. 2h,i; Supplementary Video 1). To investigate the dynamics of TSPAN4 puncta, we carried out FRAP assays on RFs and observed a rapid recovery of the TSPAN4-GFP signal after bleaching, which was largely mediated by the movement of TSPAN4 puncta (Supplementary Fig. 2d). To further validate this observation, we generated a TSPAN4-mMaple3 construct, which allowed us to carry out photoconversion experiments. As shown in Supplementary Fig. 2e, the locally converted TSPAN4-mMaple3 puncta quickly moved away from the point of conversion. Using the same imaging setting, we found that TSPAN4 puncta assembled on the migrasomal surface during the growth phase (Fig. 2j,k). The same assembly behaviour was exhibited by photoconverted TSPAN4-mMaple3 puncta (Fig. 2l).

Taken together, these experiments indicate that TSPAN4 molecules on RFs and migrasomal membranes are organized into clusters, which are highly dynamic and undergo recruitment to the migrasomal surface.

**The migrasomal membrane is a tetraspanin- and cholesterol-enriched macrodomain.** It has been well established that tetraspanin proteins form tetraspanin- and cholesterol-enriched microdomains, TEMs, on membranes<sup>7,8</sup>. We checked whether typical TEM components other than TSPAN4 are also localized on migrasomes. Indeed, we found that the migrasomes were enriched with cholesterol (Fig. 3a), a key component of TEMs<sup>9</sup>. In addition, we observed that migrasomes were enriched with other TEM components, such as integrins<sup>3</sup> and other tetraspanins (Supplementary Fig. 3a). Thus, migrasomal membranes are largely composed of TEM components. In contrast to typical TEMs, which are around 100 nm, the migrasomal membranes were several microns in size (Fig. 3a). Thus, the migrasomal membrane is a macrodomain of TEM components, particularly of tetraspanins and cholesterol. We denote these macrodomains as TEMAs.

**Cholesterol and TSPAN4 are highly enriched in migrasomes.** To evaluate the extent of TSPAN4 and cholesterol enrichment in migrasomes compared to RFs, we carried out single-molecule counting by three-dimensional (3D)-photoactivated localization microscopy (PALM). Since the z-axis depth of 3D-PALM is around 200 nm, this method enabled us to measure the number of TSPAN4 molecules in the lowest ~200-nm segment of migrasomes and RFs (Fig. 3b). Based on the calculated surface area of migrasomes and RFs in this segment, we were able to determine the concentration of TSPAN4 (Fig. 3c). We found that the concentration of TSPAN4 in migrasomes was about four times higher than in RFs (Fig. 3d).

Next, we determined the extent of enrichment of cholesterol in migrasomes compared to RFs. For this purpose, we stained

TSPAN4-GFP-expressing cells with filipin III and determined the relative enrichment of TSPAN4-GFP and cholesterol on migrasomes. We found that the migrasomal enrichment of cholesterol was tenfold larger than the enrichment in TSPAN4 (Fig. 3e,f). Using these data along with the above results of TSPAN4 enrichment, we were able to calculate that cholesterol is enriched about 40-fold in migrasomes relative to RFs (Fig. 3e).

**Cholesterol is necessary for migrasome formation.** Next, we tested whether cholesterol is required for migrasome formation. First, we treated cells with the cholesterol-depletion reagent methyl-β-cyclodextrin. We found that methyl-β-cyclodextrin treatment blocked migrasome formation (Supplementary Fig. 3b,c). To test the effect of cholesterol in a more physiologically relevant setting, we grew cells in lipoprotein-deficient serum (LPDS) with or without the HMG-CoA reductase inhibitor pravastatin. We found that both treatments substantially reduced the cellular cholesterol level (Supplementary Fig. 3d), and both treatments significantly impaired migrasome formation (Fig. 3g,h). These data reinforce the conclusion that cholesterol is a necessary component of the migrasomal domains.

**Tetraspanin and cholesterol are sufficient for migrasome formation.** To find out whether tetraspanin and cholesterol are sufficient for migrasome formation, we sought to reconstitute this phenomenon in an *in vitro* membrane system.

We purified TSPAN4-GFP (Fig. 4a) and prepared proteoliposomes embedded with TSPAN4-GFP. Next, we generated TSPAN4-containing giant unilamellar vesicles (GUVs) via electrofusion of the proteoliposomes. While most of the material generated GUVs, about 10% of it formed beads-on-a-string-like structures, which were very similar to the migrasome-bearing RFs observed in live cells (Fig. 4b). Although the membrane shape transformations driven by strong electric fields are not physiologically relevant, this result does indicate that TSPAN4-containing membranes have an intrinsic tendency to adopt configurations that are reminiscent of migrasomes on RFs. This observation motivated us to design an *in vitro* membrane setup to simulate the formation of RFs and migrasomes.

RFs are pulled out of the rear of the cell as a result of spotwise adhesion of the cell membrane to the substrate followed by migration of the cell away from the adhesion points. We imitated RF formation by pulling membrane tethers out of GUVs. To mimic the cell adhesions, we prepared cholesterol-containing GUVs with biotin-labelled phosphatidylethanolamine (PE) and attached them to the bottom of a flow chamber coated with streptavidin. For tether formation and simulation of cell migration, we used a syringe to generate a flow of liquid surrounding the GUVs, which provided a mechanical force moving the GUV body away from the adhesion points<sup>10–12</sup> (Fig. 4c). For the negative control, we used CD63, a protein of the tetraspanin family that does not induce migrasome formation after it is overexpressed (Fig. 1a).

Application of a flow to GUVs containing TSPAN4, TSPAN7 or CD63 resulted in the formation of long, thin membrane tethers similar to RFs (Fig. 4d). The tethers containing TSPAN4-GFP and TSPAN7-GFP, which were sufficient to promote migrasome formation *in vivo* (Fig. 1a), exhibited swollen regions whose shapes and sizes were similar to those of migrasomes *in vivo* (Fig. 4d). In contrast, no migrasome-like structures formed on the tethers pulled out of protein-free GUVs and of GUVs containing CD63 (Fig. 4d,e).

Next, we studied the change in distribution of TSPAN4 before and after migrasome formation. Initially, small TSPAN4 puncta were randomly distributed across the GUV membranes. After migrasome formation, the TSPAN4 puncta were highly enriched in the migrasome-like structures (Fig. 4f,g). Furthermore, cholesterol was completely colocalized with TSPAN4 in the migrasome-like structures generated in the reconstituted system (Supplementary

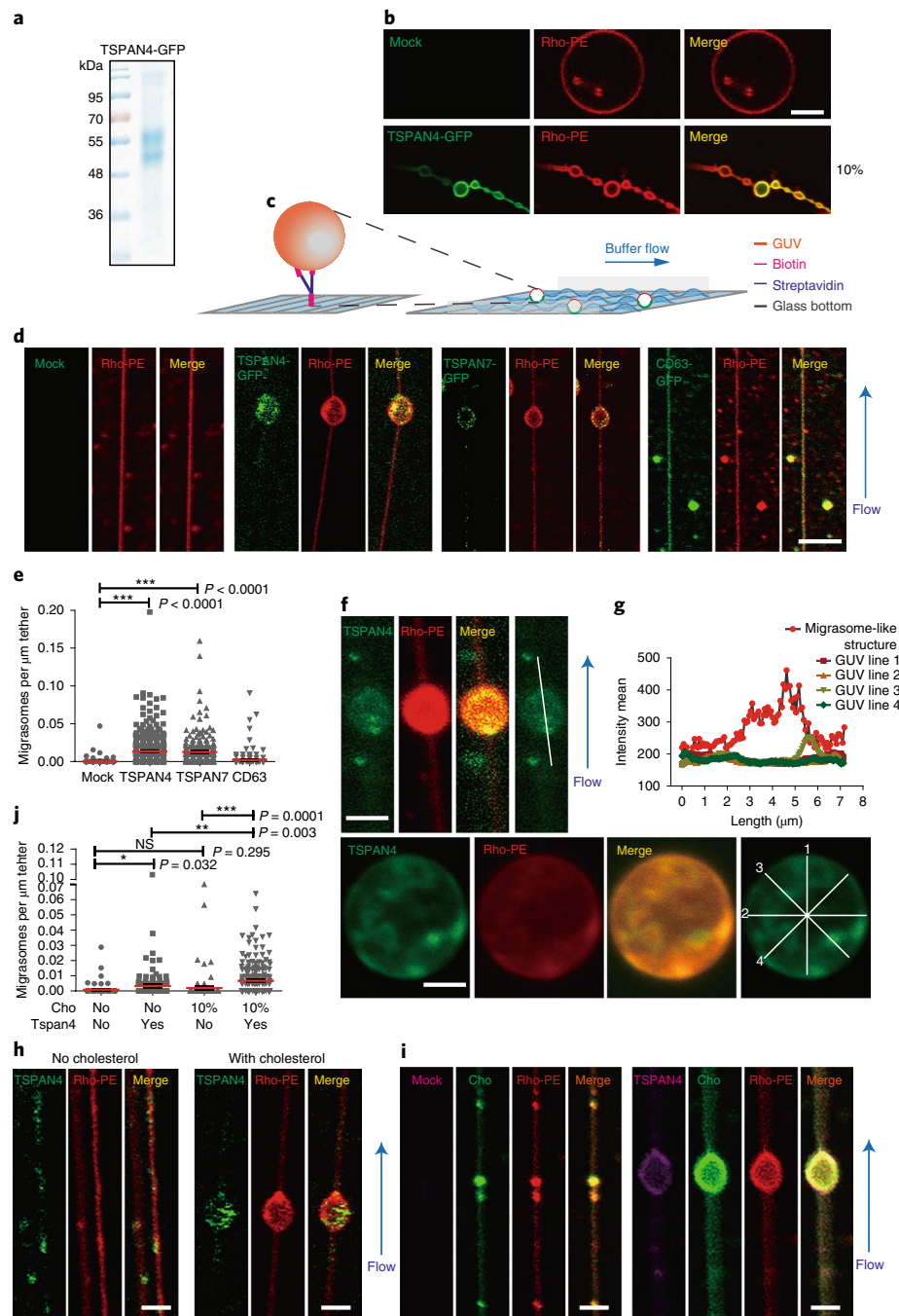


**Fig. 4 | Tetraspanin and cholesterol are sufficient for migrasome formation.** **a**, Recombinant TSPAN4-GFP was analysed on a SDS-PAGE gel and stained using Coomassie Brilliant Blue. **b**, TSPAN4-GFP proteoliposomes or liposomes were subject to electroformation to generate GUVs and visualized by confocal microscopy. Rho, rhodamine. Scale bar, 5 μm. **c**, Diagram showing the flow channel system for in vitro reconstitution of migrasomes. **d**, Control GUVs and GUVs embedded with TSPAN4-GFP, TSPAN7-GFP and CD63-GFP were subjected to the in vitro reconstitution assay as described in **c**. Green indicate proteins, red indicates rhodamine-PE. Scale bar, 5 μm. **e**, The average number of migrasomes per μm of tether from images in **d** was quantified. Data shown represent the mean ± s.e.m.; n = 256 (mock), 341 (TSPAN4), 228 (TSPAN7) and 224 (CD63) tethers. **f**, Z-stack images of TSPAN4-containing GUVs before (lower) or after (upper) the in vitro reconstitution assay. TSPAN4 was labelled with Cy5-SE (20 μg ml<sup>-1</sup>). The mean intensity z-projections were generated using ImageJ. Scale bar, 2.5 μm. **g**, Mean fluorescence intensity of TSPAN4 along the white lines in **f**. **h**, TSPAN4-GFP-containing GUVs with or without 10% cholesterol were subjected to the in vitro reconstitution assay. Scale bar, 2 μm. **i**, Control and TSPAN4-containing GUVs labelled with rhodamine-PE and Topfluor-cholesterol were subjected to the in vitro reconstitution assay. Cy5-SE was used to detect TSPAN4. Purple indicates proteins, green indicates Topfluor-cholesterol, red indicates rhodamine-PE. Scale bar, 2 μm. **j**, Quantification of the average number of migrasomes per μm of tether from images in **h** and **i**. Data shown represent the mean ± s.e.m.; n = 89 (no cholesterol (Cho.), no TSPAN4), 136 (no cholesterol, with TSPAN4), 105 (10% cholesterol, no TSPAN4) and 214 (10% cholesterol, with TSPAN4) tethers. \*\*\*P < 0.001, \*\*P < 0.01, \*P < 0.05. The unprocessed gel image related to **a** is presented in Supplementary Fig. 6. Experiments were performed three (**a** and **d–j**) or four times (**b**). Quantifications in **e** and **j** are pooled from three independent experiments with statistical details provided in Supplementary Table 4. For **g**, one representative experiment is shown. Two-tailed unpaired t-tests were used for statistical analyses.

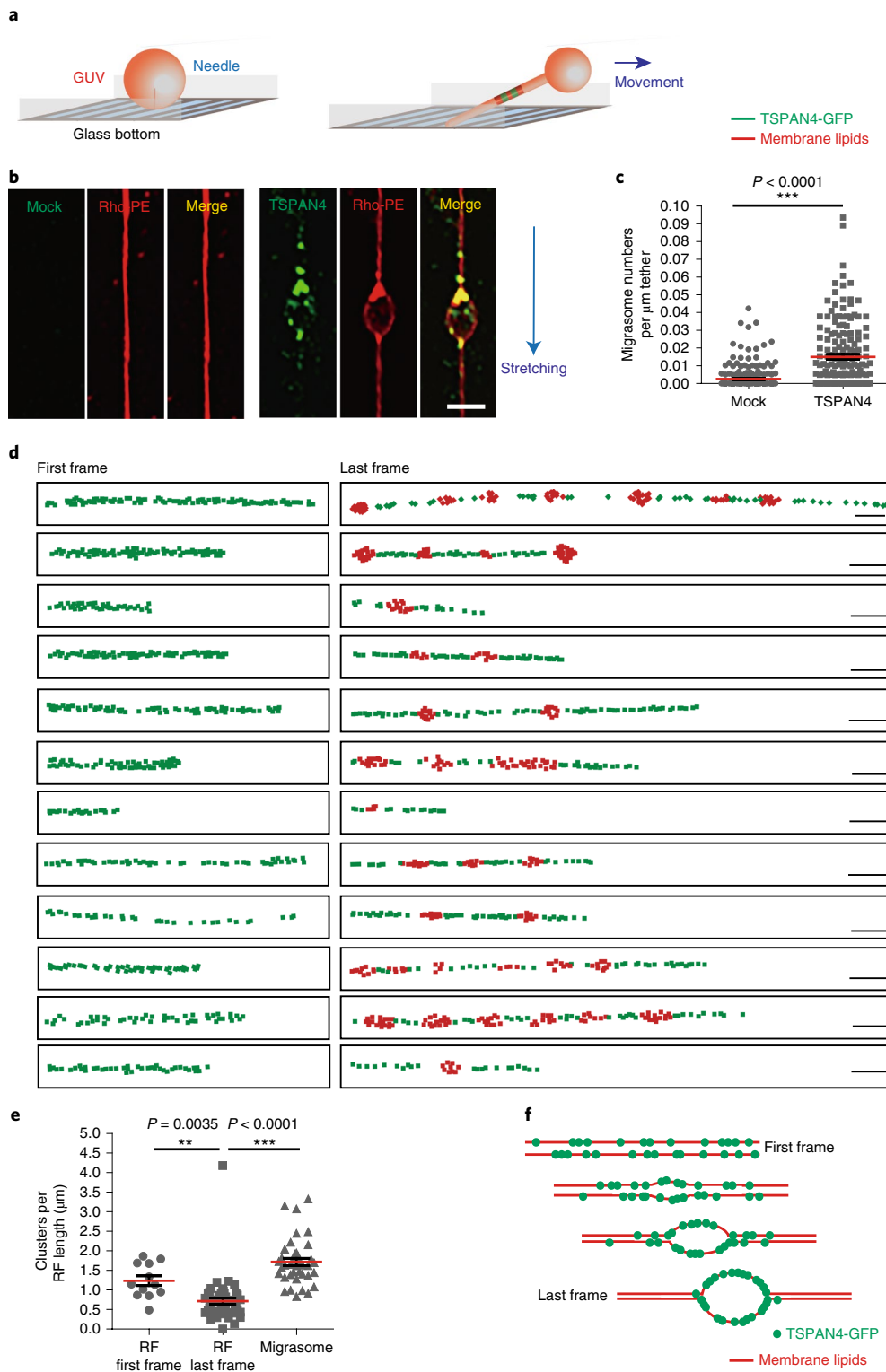


**Fig. 5 | Assembly of TEMs into TEMAs.** **a**, Diagram showing the in vitro reconstitution of migrasome formation by pulling of GUVs. **b**, Control GUVs and GUVs embedded with TSPAN4-GFP were subjected to in vitro reconstitution as described in **a**. Green indicates proteins, red indicates rhodamine-PE. Scale bar, 5  $\mu\text{m}$ . **c**, The average number of migrasomes per  $\mu\text{m}$  of membrane tether from images like those in **b** was quantified. Data shown represent the mean  $\pm$  s.e.m.;  $n = 226$  (mock) and 172 (TSPAN4) tethers. **d**, Confocal images of tether pulling reconstitutions were analysed using the software Imaris. Green spots represent TSPAN4-GFP clusters on RFs and red spots represent TSPAN4-GFP clusters on migrasomes. Scale bar, 10  $\mu\text{m}$ . **e**, Images from **d** were quantified for the number of clusters per  $\mu\text{m}$  of RF. Data shown represent the mean  $\pm$  s.e.m.  $n = 12$  for RFs in the first frame,  $n = 48$  for RFs in the last frame,  $n = 38$  for migrasomes in the last frame. \*\* $P < 0.01$ , \*\*\* $P < 0.001$ . **f**, Diagram showing the pulling force-induced assembly of TEMs. Experiments were independently repeated three (**b** and **c**) or six (**d** and **e**) times. Quantifications in **c** and **e** were pooled from these independent experiments. Two-tailed unpaired *t*-tests were used for statistical analyses. The statistical details for **c** and **e** are available in Supplementary Table 4.

Fig. 4). When cholesterol was absent from the TSPAN4-GFP-containing GUVs, the migrasome-like vesicles did not form and TSPAN4 did not assemble into micron-scale domains (Fig. 4*h,j*). Instead, small clusters of TSPAN4 were scattered along the membrane tether. Similarly, when TSPAN4 was absent from cholesterol-containing GUVs, generation of migrasome-like structures was not observed; instead, small cholesterol clusters were distributed along the membrane tether (Fig. 4*i,j*). Taken together, these data support the concept that both cholesterol and TSPAN4 are required for the assembly of TEMAs, which are required for migrasome formation.

**Assembly of TEMs into TEMAs.** To study the dynamics of TEM assembly into macromolecules, we designed a modified version of the *in vitro* migrasome formation system. Stretched membrane tethers simulating the RFs were generated by manually pulling the GUV membrane through application of a direct force to a small spot on the membrane. The force was applied by means of a glass needle attached to the membrane (Fig. 5*a*). We found that the migrasome-like structures formed on the tethers only if the GUV membrane contained TSPAN4 (Fig. 5*b,c*; Supplementary Videos 2 and 3). They did not form in the control experiments in which the GUV membranes were protein-free or contained CD63 (Fig. 5*b,c*; Supplementary Fig. 5*a*). The migrasome-like structures formed in these experiments were enriched in TSPAN4-GFP proteins (Supplementary Fig. 5*b*).

This system allowed us to carry out real-time imaging of the process of migrasome-like structure formation. As shown in Supplementary Fig. 5*b*, the pulling resulted in the elongation and narrowing of the tether, which was accompanied by the self-assembly of TSPAN4 puncta into larger clusters (Fig. 5*d,e*; Supplementary Fig. 5*c,d*). At the end of the pulling process, the initially evenly distributed TSPAN4-rich TEMs self-organized into TEMAs, which eventually underwent swelling into migrasome-like structures (Fig. 5*f*). Hence, transformation of a practically flat GUV membrane into a stretched tubule-like tether after application of a pulling force drives the formation of TEMAs, which are then shaped into migrasome-like structures.

**Model of migrasome formation.** To understand the physical basis for the generation of migrasomes from TEMAs, we developed a theoretical model. Our hypothesis is that shaping of a migrasome, whose mid-cross-section is substantially wider than that of the RF tubule, is due to the difference between the elastic properties of TEMAs and those of the RF membrane. More specifically, we propose that the major factor that drives the swelling of a TEMA into a migrasome-like structure is a considerable increase in the TEMA membrane-bending modulus,  $\kappa_p$ , compared to that of the RF membrane,  $\kappa_m$ , which results from enrichment of the domain in cholesterol and tetraspanin. We further suggest that additional factors, which guarantee that the migrasome adopts a sphere-like rather than a barrel-like shape, act to contract the two boundaries of a TEMA, hence counteracting the general tendency of the TEMA membrane to swell. We consider these factors to be the line tension of the TEMA boundaries,  $\lambda$ , and/or the difference between the moduli of the Gaussian curvature of the TEMA,  $\bar{\kappa}_p$ , and RF,  $\bar{\kappa}_m$ , membranes.

We consider the following scenario of migrasome formation. First, a RF is pulled out of the body of a moving cell as a result of a local attachment of the cell plasma membrane to the substrate and the subsequent movement of the cell along the substrate away from the attachment point (Fig. 6*a*). The membrane of the resulting RF is subject to a lateral tension, which is directly related to the tension,  $\gamma_0$ , existing in the cell plasma membrane. Second, assembly of TEMs along a finite fragment of the RF gives rise to a TEMA (Fig. 6*b*). We consider the TEMA to be separated from the rest of the RF by two effective boundary lines, at which the tetraspanin and cholesterol concentrations abruptly drop from large to negligibly

small values (Fig. 6*b*). The TEMA region transforms into a migrasome by changing its shape while remaining embedded in the RF between the same boundaries (Fig. 6*c*). In the following, the TEMAs and the rest of the initial membrane tether will be referred to as the migrasomal membrane and the RF membrane, respectively.

Migrasome formation is driven by the interplay of the following three energy contributions: the bending energies of the migrasomal and RF membranes, the energy of the membrane tension, and the energy of the migrasome–RF boundary.

The qualitative essence and the mathematical details of the model are presented in Supplementary Note 1. The computational results are presented in Fig. 6*e,f*.

A general conclusion following from the results presented in Fig. 6*e* is that a high bending modulus of the tetraspanin-enriched membrane of the migrasome,  $\kappa_p$ , can indeed be the origin of the migrasomal shape, provided that either the migrasome–RF boundary possesses a large enough line tension,  $\lambda$ , or the difference between the moduli of Gaussian curvature of the RF and migrasomal membranes,  $\bar{\kappa}_m - \bar{\kappa}_p$ , is positive and sufficiently large.

To estimate the required values of these parameters, we determined the average sphericity,  $\beta_a$  (see Supplementary Note 1 for a definition) of the computed migrasomal shapes and compared them with the sphericities of the experimentally observed migrasomes. The predicted average sphericity is presented in Fig. 6*f* as a function of the ratio between the bending moduli of the migrasomes and RFs,  $\kappa_p/\kappa_m$ , and the normalized values of either the boundary line tension,  $\lambda$  (Fig. 6*e*), or the difference between the moduli of Gaussian curvature,  $\Delta\bar{\kappa} = \bar{\kappa}_m - \bar{\kappa}_p$  (Fig. 6*e*). The broken lines in the charts presented in Fig. 6*f* correspond to the maximal and minimal average sphericity of the artificial migrasomes observed to form on tethers pulled out of the TSPAN4-containing GUVs (Supplementary Fig. 5*b*).

The results presented in Fig. 6 emphasize that, according to our model, generation of the experimentally observed shapes of migrasomes requires the bending modulus of the migrasomal membrane to exceed that of the membrane of the RFs by a factor in the range between five and ten, and the boundary factors,  $\lambda$  and/or  $\bar{\kappa}_m - \bar{\kappa}_p$ , to have considerable values.

**Membrane stiffening by TSPAN4 and cholesterol.** According to the predictions of our model, to guarantee that a TEMA reaches a degree of sphericity within the experimentally observed range, the domain-bending modulus has to exceed that of the lipid membrane by a factor of five to ten (Fig. 6*e*, II, III).

To experimentally substantiate this proposal, we directly measured the bending modulus of proteoliposomes containing elevated concentrations of TSPAN4 and cholesterol. For the measurements, we used atomic force microscopy (AFM) (Fig. 7*a*), as suggested in a previous study<sup>13</sup>. In this method, the membrane-bending rigidity is derived from the measured relationship between the compressing force,  $f$ , applied to the liposome apex by the cantilever tip, and the resulting flattening of the liposome quantified by the length of the apex shift,  $D$ . For deformations in which the deformation length,  $D$ , is much smaller than the initial liposome radius,  $R$ , such that  $\frac{D}{R} \ll 1$ , the experimentally determined force-deformation relationship (Fig. 7*b*),  $f(D)$ , enabled us to compute of the effective liposome stiffness,  $K_1$ , according to the following equation:

$$K_1 = \frac{df}{dD} \quad (1)$$

The membrane-bending rigidity,  $\kappa$ , is related to the liposome stiffness as follows<sup>13</sup>:

$$\kappa = K_1 R - \frac{h\sqrt{3}}{48\sqrt{1-\nu^2}} \quad (2)$$

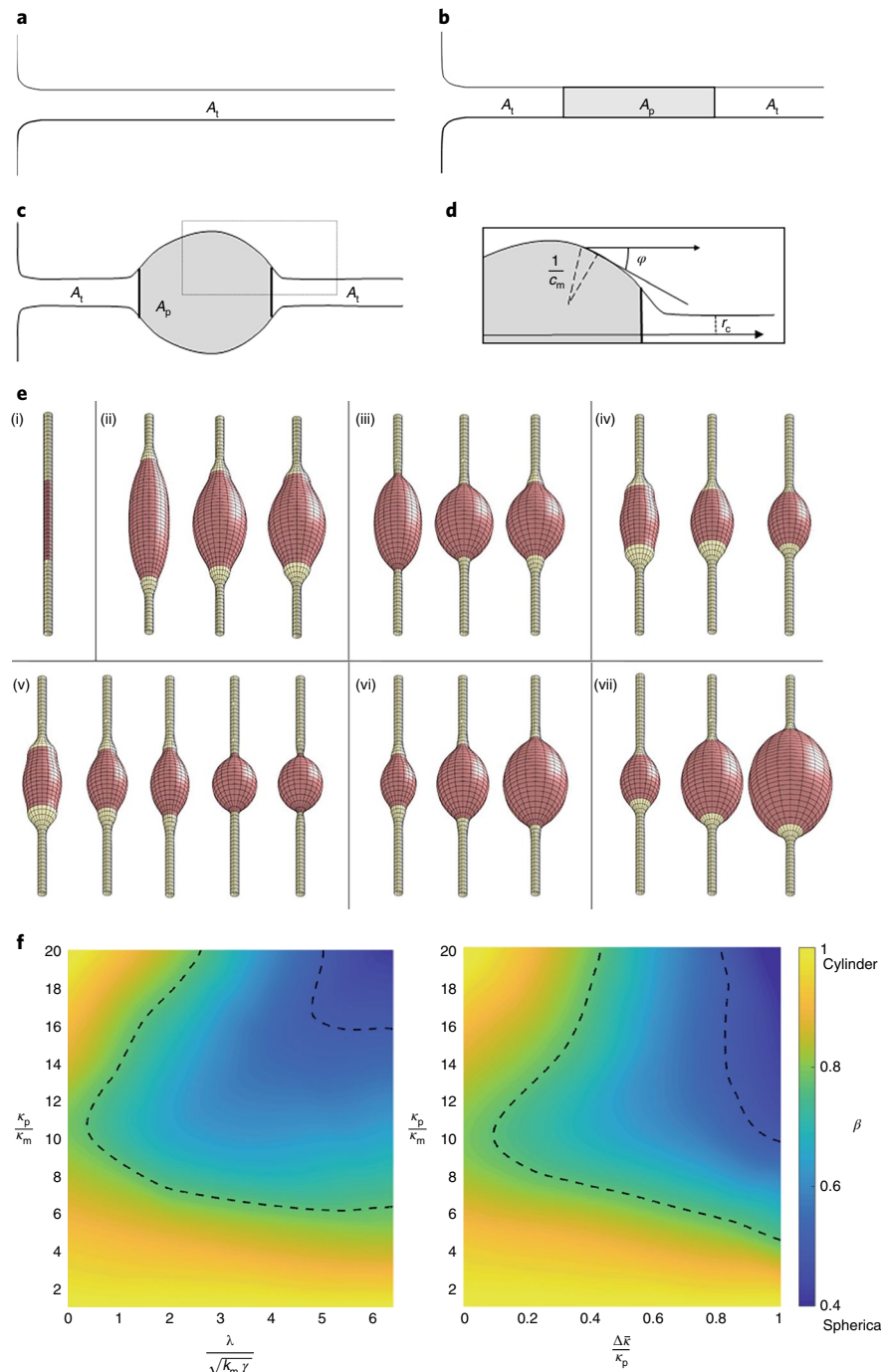


**Fig. 6 | Model of migrasome formation.** **a-d**, Cartoons illustrating the model and notations. **a**, A tubular RF of area  $A_t$  pulled out of the cell membrane. **b**, Tetraspanin and cholesterol molecules concentrate within a specified surface area of the RF, denoted by  $A_p$ . On the edge of this region, the concentration of tetraspanin and cholesterol molecules drops sharply from substantial to negligible. **c**, The tetraspanin/cholesterol-rich surface transforms into a migrasome. **d**, Enlargement of a migrasome fragment (boxed region in **c**). **e**, Results of computations. Model (i) shows that the migrasomal and RF membranes are identical,  $\kappa_p = \kappa_m$ ,  $\bar{\kappa}_m = \bar{\kappa}_p$ ,  $\lambda = 0$ . Model (ii) shows that the bending rigidity ratios,  $\kappa_p/\kappa_m$ , adopt values of 4, 7 and 10 for vanishing line tension,  $\lambda = 0$ , and equal moduli of Gaussian curvature,  $\bar{\kappa}_m = \bar{\kappa}_p$ . Model (iii) shows that the bending rigidity ratios adopt values of 5, 10 and 15 for the line tension  $\lambda = 3.4\sqrt{\kappa_m \gamma_0}$ , migrasome area  $A_p = 350\frac{\kappa_m}{\gamma_0}$  and  $\bar{\kappa}_m = \bar{\kappa}_p$ . Model (iv) shows that the difference of Gaussian curvature moduli,  $\Delta \bar{\kappa} = \bar{\kappa}_m - \bar{\kappa}_p$ , adopts values of 0, 0.5  $\kappa_p$ , and  $\kappa_p$  for  $A_p = 200\frac{\kappa_m}{\gamma_0}$ ,  $\lambda = 0$  and  $\kappa_p = 10\kappa_m$ . Model (v) shows that the line tension,  $\lambda$ , adopts values of 0,  $3\sqrt{\kappa_m \gamma_0}$ ,  $5\sqrt{\kappa_m \gamma_0}$ ,  $7\sqrt{\kappa_m \gamma_0}$  and  $9\sqrt{\kappa_m \gamma_0}$  for  $A_p = 200\frac{\kappa_m}{\gamma_0}$ ,  $\kappa_p = 10\kappa_m$  and  $\bar{\kappa}_m = \bar{\kappa}_p$ . Model (vi) shows that the migrasome area adopts values of  $150\frac{\kappa_m}{\gamma_0}$ ,  $300\frac{\kappa_m}{\gamma_0}$  and  $450\frac{\kappa_m}{\gamma_0}$  for  $\lambda = 0.7\sqrt{\kappa_m \gamma_0}$ ,  $\kappa_p = 10\kappa_m$  and  $\bar{\kappa}_m = \bar{\kappa}_p$ . Model (vii) shows that the migrasome area,  $A_p$ , adopts values of 150, 400 and 700  $\frac{\kappa_m}{\gamma_0}$  for  $\bar{\kappa}_m - \bar{\kappa}_p = \kappa_p - \kappa_m$ ,  $\kappa_p = 10\kappa_m$  and  $\lambda = 0$ . **f**, Results of the computations show the dependence of the migrasomal shape sphericity,  $\beta$ , on the model parameters. The sphericity is represented in colours as indicated in the colour bar, with yellow representing cylindrical and blue representing spherical. The vertical axis represents the bending rigidity of the protein cluster divided by that of the membrane,  $\frac{\kappa_p}{\kappa_m}$ . Left: the horizontal axis represents the normalized line tension,  $\frac{\lambda}{\sqrt{\kappa_m \gamma_0}}$  for  $\bar{\kappa}_m - \bar{\kappa}_p = 0$ . Right: the horizontal axis represents  $\frac{\Delta \bar{\kappa}}{\kappa_p}$  for  $\lambda = 0$ . The two broken curves in these two charts represent the minimal and maximal sphericity of the migrasomal shapes observed in the tether-pulling experiments. All of the simulation results correspond to a constant migrasomal area  $A_p = 400\frac{\kappa_m}{\gamma_0}$ .

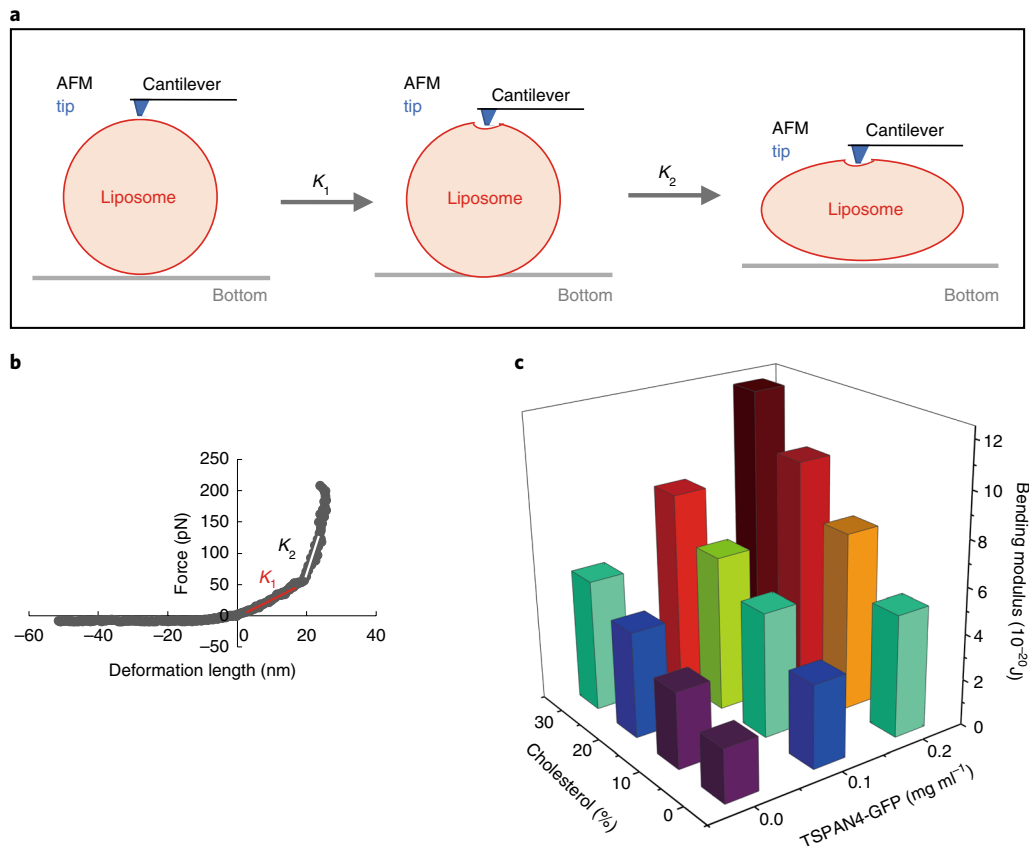


**Fig. 7 | Membrane stiffening by TSPAN4 and cholesterol.** **a**, Diagram of the method for measuring the membrane-bending rigidity by AFM. **b**, Typical ‘force to deformation length’ trace from an AFM experiment.  $K$  is the slope after linear fitting. The typical trace is a representative of 1,044 traces for proteoliposomes (containing  $0.1\text{ mg ml}^{-1}$  TSPAN4-GFP and 10% cholesterol) from 3 independent experiments. **c**, 3D-histogram showing the bending moduli of liposomes with different concentrations of TSPAN4-GFP and cholesterol. Exact values related to **c** are presented in Table 1, and the statistical details are available in Supplementary Tables 2–4.

**Table 1 | Bending moduli of liposomes with different concentrations of TSPAN4 and cholesterol**

		Cholesterol (%)			
		0	10	20	30
TSPAN4-GFP( $\text{mg ml}^{-1}$ )	0	2.3	3.3	4.6	5.7
	0.1	3.6	5.4	6.7	8.5
	0.2	5.3	7.7	9.9	12.2

Bending rigidity ( $10^{-20}$  J) was calculated from AFM force-deflection response using equation (2). Data shown represent the average of three independent experiments.

where  $h$  is the membrane thickness and  $\nu$  is the membrane Poisson ratio. To determine the bending modulus according to equations (1) and (2), we used the typical value of the thickness  $h=4\text{ nm}$  and the generic value of  $\nu=0.5$ , thus implying a volume incompressibility of the membrane material<sup>14</sup>.

The measurement results presented in Table 1, Supplementary Tables 2 and 3 and Fig. 7c show that an increase in the membrane TSPAN4 concentration from 0 to  $0.2\text{ mg ml}^{-1}$  and of the cholesterol content from 0 to 30% resulted in the growth of the membrane-bending modulus by a factor of about five. According to the model predictions, such an increment of the bending rigidity,  $\kappa$ , is already sufficient to form the migrasome-like shape<sup>15</sup>. Moreover, our results suggest a monotonic increase of  $\kappa$  with the TSPAN4 and cholesterol concentrations. This implies that the values of the bending modulus in migrasomes are even larger than those reached in our experiment.

Indeed, as shown above, the TSPAN4 and cholesterol concentrations in migrasomes exceeded those in RFs by factors of 4 and 40, respectively, which is greatly beyond the concentration ranges we could reach in proteoliposomes. Hence, the migrasomal bending rigidity must substantially exceed the values presented in Table 1, which further strengthens the validity of our model.

## Discussion

In this study, we found that TSPAN4 and cholesterol are necessary for migrasome formation *in vivo*. Moreover, we simulated the process of migrasome formation using an *in vitro* system. In this system, we were able to show that TSPAN4 and cholesterol are sufficient for the formation of migrasome-like structures. We revealed that migrasome formation is mediated by the assembly of 100-nm-scale TEMs, which exist in the tether membrane, into micron-scale macromodules (TEMAs). The latter swell into the large vesicle-like migrasomal shape.

To explain this observation, we developed a theoretical model whereby the swelling of TEMAs into the migrasomal shape is due to the substantially elevated bending stiffness of TEMAs compared to that of RFs. A clue for an intuitive understanding of this effect is given in Supplementary Note 1. We propose and support experimentally that the high degree of bending stiffness is a consequence of the strong enrichment of cholesterol and tetraspanin in TEMAs.

We computationally derived and experimentally substantiated that the bending modulus of the cholesterol- and tetraspanin-rich membrane of a migrasome must be five to ten times larger than that of the RF. This is in good agreement with literature data. Indeed,

a recent study<sup>16</sup> demonstrated that the large cholesterol concentrations corresponding to the liquid-ordered state of a membrane augment the membrane-bending modulus by a factor of ten. Moderate increases of cholesterol concentrations up to about 30 mole percent lead to the growth of bending moduli by a factor of up to about four<sup>17</sup>. In addition, enrichment in proteins is also supposed to increase the membrane-bending stiffness, but to a relatively modest extent<sup>18</sup>.

Our model predicted that, besides the membrane-bending modulus, an important role in migrasome formation is played by the forces that act on the boundary between the migrasome and RF. That is, the boundary line tension,  $\lambda$ , and/or the difference between the moduli of Gaussian curvature,  $\Delta\bar{\kappa} = \bar{\kappa}_m - \bar{\kappa}_p$ . Although we were not able to directly measure the TEMA line tension,  $\lambda$ , its values predicted by our model are within the range described in the literature. For generality, we presented in Fig. 6e, model (v), the line tension values in dimensionless units. Converting them into physical units (pN) by using the typical bending rigidity of the RF membrane,  $\kappa_m = 10^{-19}$  joule (J), and the membrane tension,  $\gamma = 2\frac{\lambda N}{m}$ , corresponding to the 100-nm diameter of a RF, we found that the line tension values required by the model are in the range between 0.6 pN and 6.0 pN. Experimental studies have provided lipid domain line tensions in the range between 0.5 and 3.3 pN<sup>19</sup>. Based on the theoretical evaluation<sup>20</sup> for a domain with a bending rigidity that is four times larger than that of the surrounding bilayer, the domain line tension can be expected to reach 6 pN.

Our model predicted a range between 0.2 and 1.0 for another elastic parameter of the membrane,  $\frac{\Delta\bar{\kappa}}{\kappa_p}$ , where  $\Delta\bar{\kappa}$  is the difference between the moduli of Gaussian curvature of the RF membrane and the migrasome, and  $\kappa_p$  is the bending modulus of the migrasome membrane. This is in good agreement with the experimental data on the difference between the moduli of Gaussian curvature of liquid-disordered and liquid-ordered phases constituting  $\Delta\bar{\kappa} \cong 3.6 \times 10^{-19}$  J<sup>21</sup>. In fact, provided that the bending modulus of the migrasome membrane equals  $\kappa_p = 10^{-18}$  J, our model predicts (Fig. 6f) that the range of  $2 \times 10^{-19}$  J <  $\Delta\bar{\kappa} < 10^{-18}$  J, which corresponds to the migrasome formation<sup>21</sup>.

Migrasomes on RFs are reminiscent of the structures formed as a result of pearling instability as described for cellular membrane tubules exposed to tension<sup>22</sup> or covered by grafted polymers<sup>23</sup>. This raises the possibility that migrasome formation may result from Rayleigh-like instability of the RFs<sup>22</sup> or from spontaneous curvature of the membrane induced by tetraspanins or other molecules.

Rayleigh-like instability does not seem relevant to our system. Indeed, an essential condition for Rayleigh instability is the conservation of the volume within the tubule<sup>22,24</sup>. This condition does not hold in our system since, according to our observations<sup>2</sup>, the luminal volume of the tubules is freely and quickly exchangeable with the cell body. A partial volume conservation may occur on short time scales, but our observations are so long that there are definitely no time limitations on the water exchange between the RF and the cell interior or the extracellular space. Moreover, Rayleigh pearling instability is generic and must therefore be independent of the presence of protein on the membrane surface, while the formation of migrasome depends on the presence of TSPAN4 and cholesterol.

Also, the spontaneous curvature mechanism of pearling as suggested in a previous study<sup>23</sup> is irrelevant for our system. The pearling transition in that study was the result of the spontaneous curvature generated by grafted polymers when the membrane area-to-volume ratio was constant. In our system, the area-to-volume ratio is not constant because of the volume exchange.

Our data showed that TSPAN4 forms puncta on RFs, which concentrate into a dense domain on the migrasomal surface. Since the size and dynamics of TSPAN4-GFP puncta are similar to those of TEMs, we suggested that the TSPAN4 puncta represent TEMs. However, TEMs should contain cholesterol, while very little cholesterol signal was observed in RFs. One possible explanation for this result could be

that the sparsely distributed TEMs on RFs contain a small amount of cholesterol, which is below the detection limit of filipin III staining. When a large number of TEMs are densely packed into a TEMA, the cholesterol becomes detectable by staining with filipin III.

In contrast to cholesterol, we did observe a considerable amount of TSPAN4 on the RFs. A possible explanation for this phenomenon is that while practically all the cholesterol in RFs is located in TEMs, tetraspanins are partitioned between TEMs and free molecules. The free TSPAN4 molecules would not be concentrated in TEMAs, thus stay in RF.

## Online content

Any methods, additional references, Nature Research reporting summaries, source data, statements of code and data availability and associated accession codes are available at <https://doi.org/10.1038/s41556-019-0367-5>.

Received: 6 September 2018; Accepted: 28 June 2019;

Published online: 1 August 2019

## References

- Taylor, A. C. & Robbins, E. Observations on microextensions from the surface of isolated vertebrate cells. *Dev. Biol.* **6**, 660–673 (1963).
- Ma, L. et al. Discovery of the migrasome, an organelle mediating release of cytoplasmic contents during cell migration. *Cell Res.* **25**, 24–38 (2015).
- Wu, D. et al. Pairing of integrins with ECM proteins determines migrasome formation. *Cell Res.* **27**, 1397–1400 (2017).
- Jiang, D. et al. Migrasomes provide regional cues for organ morphogenesis during zebrafish gastrulation. *Nat. Cell Biol.* <https://doi.org/10.1038/s41556-019-0358-6> (2019).
- Rubinstein, E. The complexity of tetraspanins. *Biochem. Soc. Trans.* **39**, 501–505 (2011).
- Charrin, S. et al. Lateral organization of membrane proteins: tetraspanins spin their web. *Biochem. J.* **420**, 133–154 (2009).
- Zuidzherwoude, M. et al. The tetraspanin web revisited by super-resolution microscopy. *Sci. Rep.* **5**, 12201 (2015).
- Le Naour, F., Andre, M., Boucheix, C. & Rubinstein, E. Membrane microdomains and proteomics: lessons from tetraspanin microdomains and comparison with lipid rafts. *Proteomics* **6**, 6447–6454 (2006).
- Hemler, M. E. Tetraspanin proteins mediate cellular penetration, invasion, and fusion events and define a novel type of membrane microdomain. *Ann. Rev. Cell Dev. Biol.* **19**, 397–422 (2003).
- Borghi, N., Rossier, O. & Brochard-Wyart, F. Hydrodynamic extrusion of tubes from giant vesicles. *Europhys. Lett.* **64**, 837–843 (2003).
- Rossier, O. et al. Giant vesicles under flows: extrusion and retraction of tubes. *Langmuir* **19**, 575–584 (2003).
- Solon, J., Streicher, P., Richter, R., Brochard-Wyart, F. & Bassereau, P. Vesicles surfing on a lipid bilayer: self-induced haptotactic motion. *Proc. Natl Acad. Sci. USA* **103**, 12382–12387 (2006).
- Delorme, N. & Fery, A. Direct method to study membrane rigidity of small vesicles based on atomic force microscope force spectroscopy. *Phys. Rev. E Stat. Nonlin. Soft Matter Phys.* **74**, 030901 (2006).
- Landau, L. D. & Lifshitz, E. M. *Theory of Elasticity* 1st edn, Vol. 7 (Butterworth-Heinemann, 1959).
- Dimova, R. Recent developments in the field of bending rigidity measurements on membranes. *Adv. Colloid Interface Sci.* **208**, 225–234 (2014).
- Usery, R. D. et al. Membrane bending moduli of coexisting liquid phases containing transmembrane peptide. *Biophys. J.* **115**, 164 (2018).
- Oradd, G., Shahedi, V. & Lindblom, G. Effect of sterol structure on the bending rigidity of lipid membranes: a <sup>3</sup>H NMR transverse relaxation study. *Biochim. Biophys. Acta* **1788**, 1762–1771 (2009).
- Aimon, S. et al. Membrane shape modulates transmembrane protein distribution. *Dev. Cell* **28**, 212–218 (2014).
- Tian, A., Johnson, C., Wang, W. & Baumgart, T. Line tension at fluid membrane domain boundaries measured by micropipette aspiration. *Phys. Rev. Lett.* **98**, 208102 (2007).
- Kuzmin, P. I., Akimov, S. A., Chizmadzhev, Y. A., Zimmerberg, J. & Cohen, F. S. Line tension and interaction energies of membrane rafts calculated from lipid splay and tilt. *Biophys. J.* **88**, 1120–1133 (2005).
- Baumgart, T., Das, S., Webb, W. W. & Jenkins, J. T. Membrane elasticity in giant vesicles with fluid phase coexistence. *Biophys. J.* **89**, 1067–1080 (2005).
- Bar-Ziv, R. & Moses, E. Instability and “pearling” states produced in tubular membranes by competition of curvature and tension. *Phys. Rev. Lett.* **73**, 1392–1395 (1994).
- Tsafrir, I. et al. Pearling instabilities of membrane tubes with anchored polymers. *Phys. Rev. Lett.* **86**, 1138–1141 (2001).

24. Bar-Ziv, R., Tlusty, T., Moses, E., Safran, S. A. & Bershadsky, A. Pearlring in cells: a clue to understanding cell shape. *Proc. Natl Acad. Sci. USA* **96**, 10140–10145 (1999).

### Acknowledgements

The authors are grateful to members of the Kozlov and Yu groups for helpful discussions. This research was supported by the Ministry of Science and Technology of the People's Republic of China (2016YFA0500202 and 2017YFA0503404) to L.Y., the National Natural Science Foundation of China (31430053 and 31621063), the Natural Science Foundation of China international cooperation and exchange program (31561143002), the Independent Research of Tsinghua University (20161080135) to L.Y., and the Israel Science Foundation grant 1066/15, EU consortium InCeM to M.M.K., who also holds the Joseph Klafter Chair in Biophysics.

### Author contributions

L.Y., Y.H., S.Z., Y.S. and J.L. conceived the experiments. M.M.K. and B.Z. conceived the modelling. L.Y. and M.M.K. wrote the paper and supervised the project. Y.H.,

S.Z., Y.Z., H.C., T.D. and Y.L. carried out the experiments. B.Z. and S.E. performed the computations. All authors discussed the manuscript, commented on the project and contributed to preparing the paper.

### Competing interests

The authors declare no competing interests.

### Additional information

**Supplementary information** is available for this paper at <https://doi.org/10.1038/s41556-019-0367-5>.

**Reprints and permissions information** is available at [www.nature.com/reprints](http://www.nature.com/reprints).

**Correspondence and requests for materials** should be addressed to M.M.K. or L.Y.

**Publisher's note:** Springer Nature remains neutral with regard to jurisdictional claims in published maps and institutional affiliations.

© The Author(s), under exclusive licence to Springer Nature Limited 2019

## Methods

**Constructs and cell culture.** *Plasmid construction.* Complementary DNAs of tetraspanins were cloned into pEGFP-N<sub>1</sub>, pmCherry-N<sub>1</sub> or mMaple3-N<sub>1</sub> for imaging; cDNAs of tetraspanins were cloned into pCAG-strep for protein purification. All TSPAN genes were originally cloned from rat (including all 33 TSPANs) and human (TSPAN4 for protein purification) cDNAs.

**For cell lines.** Adherent cells, including NRK, MGC-803 and L929 cells and their derivatives, were cultured at 37°C and 5% CO<sub>2</sub> in DMEM growth medium supplemented with 10% serum and 1% penicillin–streptomycin. Suspensions of 293F cells were cultured at 37°C, 8% CO<sub>2</sub> and 125 r.p.m. in SMM293-TI supplemented with 1% penicillin–streptomycin.

**Cell transfection.** For NRK cells, MGC-803 cells and their derivatives, one-third of a 6-cm dish of cells was transfected with 2 µg DNA via Amaxa nucleofection using solution T and program X-001, and then grown for 15 h for protein expression. For L929 cells, a 3.5-cm dish of cells was transfected with 4 µg DNA using a Lipofectamine-3000 transfection kit (Invitrogen) and then grown for 15–18 h for protein expression. For purification of TSPAN4-GFP, 1 litre of 293F cells was transfected by adding 2 mg DNA with 3 mg polyethylenimine (1 mg ml<sup>-1</sup>).

**Generation of TSPAN4 knockout cell lines.** The *TSPAN4* gene in MGC-803 cells and NRK was deleted by a modified PX458 plasmid (provided by W. Guo from Zhejiang University) that contains two guide RNAs coupled with Cas9 nuclease. Compared with mutations generated by single guide RNAs (sgRNAs), mutations generated by targeting with dual sgRNAs are more likely to yield visibly shorter PCR fragments when amplified from genomic DNA. The sgRNA sequences used for CRISPR-Cas9 were 5'-GCTGCACGTGTCGGATACG-3' (sgRNA-1) and 5'-GCGACCAACATGGACGCCAC-3' (sgRNA-2) for MGC-803 cells, 5'-GATGGGGCGTCCGGAGCAC-3' (sgRNA-3) and 5'-GCGCACCGTGCACAGACC-3' (sgRNA-4) for NRK cells. After 72 h of transfection, the cells were seeded into 96-well plates by fluorescence-activated cell sorting (FACS) for enhanced GFP signal. DNA fragments containing the sgRNA-targeted region were amplified from genomic DNA of these monoclonal cells and sequenced to pick out the correct clones.

**Protein purification.** pCAG-strep-Tspan4-GFP or pCAG-strep-Tspan4 plasmids were transfected into 293F cells using a polyethylenimine-based transfection protocol. For transfection of 1 litre of 293F cells, 2 mg DNA was used. Transfected 293F cells were collected 3 days after transfection and lysed using a Dounce tissue grinder (100 strokes) in buffer containing 25 mM Tris-HCl (pH 8.0), 150 mM NaCl and protease inhibitor cocktail (Roche). After centrifugation at 30,000 g for 1 h at 4°C, the pellet was lysed in buffer containing 25 mM Tris-HCl (pH 8.0), 150 mM NaCl, 2% Fos-Choline-12 (Anatrace) and protease inhibitor cocktail (Roche) for 2 h at 4°C. After centrifugation at 30,000 g for 30 min, the supernatant was loaded onto a column containing Strep-Tactin resin (IBA) and incubated for 1 h at 4°C. The resin was then washed four times. The protein was eluted with 10 mM desthiobiotin (Sigma) and further purified by gel filtration on Superdex 200.

**Liposome preparation and protein insertion.** *Preparation of small unilamellar vesicles.* POPC (1-palmitoyl-2-oleyl-glycero-3-phosphocholine), DOPE (1,2-dioleoyl-sn-glycero-3-phosphoethanolamine), POPS (1-palmitoyl-2-oleyl-sn-glycero-3-phospho-L-serine), DOPE-rhodamine and PE-biotin were purchased from Avanti Polar Lipids. Cholesterol was purchased from Sigma. Lipids were mixed as POPC:DOPE:POPS:cholesterol (4:2.5:2.5:1) with 0.1% DOPE-rhodamine and 1% PE-biotin. The mixtures were dried with a nitrogen stream and further dried for 1 h at 37°C. The lipid film was then hydrated completely with HEPES buffer I (20 mM HEPES, pH 7.4, 150 mM NaCl) and subjected to 10 cycles of freezing in liquid nitrogen and thawing in a 42°C water bath. Finally, the liposomes were extruded 21 times through 1,000-nm pore size polycarbonate film to produce the small unilamellar vesicles (SUVs).

**Protein insertion.** Fos-Choline-12 (0.1%) was added to loosen SUV membranes at 4°C for 30 min, and then proteins were added to the system with 35 r.p.m. rotation at 4°C for 1 h. Finally, the Fos-Choline-12 was removed by adding 8–15 µg BIO-beads (Bio-Rad) per 100 µl system. This was repeated four times. The supernatant was frozen in liquid nitrogen and stored at –80°C.

**Preparation of GUVs with embedded proteins.** GUVs with embedded proteins were prepared from protein-containing SUVs using a Vesicle Prep-Pro machine (Nanion). First, a 20-µl drop of SUVs was coated onto indium-tin-oxide-covered glass slides to form a lipid–protein film and dried for 30 min. The slides were placed into the Vesicle Prep-Pro machine and 270 µl of 300 mM sorbitol buffer was applied onto the slides. Electroformation was then carried out at 0.24 V and 9.9 Hz for 90 min at 37°C. The GUVs were collected after cooling down to room temperature and stored at 4°C to be used within 3 days.

**Migrasome reconstitution assay via flow channel.** The flow channels were prepared as for the previously published motility assay using hydrophilic

coverslips<sup>25–27</sup>. The channels were blocked by 10% BSA:1% BSA-biotin (Amresco) at room temperature for 10 min. Then, streptavidin (0.25 mg ml<sup>-1</sup>) was loaded into each channel and incubated at room temperature for 5 min. GUVs (15 µl) were then incubated in the channels for 2 min at room temperature. Finally, 60 µl of HEPES buffer I was flowed through the channel. Images were acquired using an Olympus FV-1000 confocal microscope.

For the migrasome reconstitution assay on GUVs with embedded TSPAN4 protein, Cy5-SE (20 µg ml<sup>-1</sup>; Solarbio) was used to label the proteins at room temperature for 15 min before GUVs were loaded into the channel.

**Migrasome reconstitution assay via tether pulling.** The home-made chamber was first blocked using 1% BSA in HEPES buffer I for 10 min, then closed with mineral oil. GUVs (10 µl) were injected into each chamber. When the GUVs became stable in the system, a glass needle was inserted into the chamber and attached to the target GUV. Finally, the glass needle was pulled to one side to deform the GUV, and time-lapse images were recorded at the same time using an Olympus FV-1000 confocal microscope in free-run mode with an image size of 512 × 512 pixels.

**FRAP assay.** All the FRAP experiments were conducted under galvanometer scanning mode using a NIKON A1 confocal microscope fitted with a ×100 oil objective and three times zoom in. The area of interest area was bleached with a 480 nm laser with 20% output for 1 s. Immediately after bleaching, the laser power was decreased to 2%, and each field of 512 × 512 pixels was imaged for 10 min.

**Cell imaging and image analysis.** Confocal snapshot images were acquired using a Fluoview 1000 confocal microscope (Olympus), a ×60 objective and Fluoview 1000 software. Images were collected at 1,024 × 1,024 pixels. Confocal images of GUVs were collected using a Fluoview 1200 confocal microscope (Olympus) and a ×60 objective. Images were collected at 512 × 512 pixels. Long-term time-lapse images of living cells were collected using a NIKON A1 microscope (under galvanometer scanning mode) and a ×60 objective. Images were collected at 1,024 × 1,024 pixels. Fluorescence intensities of snapshot images were analysed using Fiji, and statistical analyses were conducted using Graphpad Prism 5. Series of z-stack images were analysed using Fiji to conduct z-projection and subsequent analyses.

To compare galvanometer scanning with resonant scanning, galvanometer scanning mode imaging was conducted by choosing the “Galvano mode” on a NIKON A1 microscope, using a ×100 objective. Images were collected at 512 × 512 pixels, 1 frame s<sup>-1</sup>, no-delay setting. Resonant scanning mode imaging was conducted by choosing the “Resonant mode” on the NIKON A1 microscope, using a ×100 objective. Images were collected at 512 × 512 pixels, 30 frames s<sup>-1</sup>, 1-s interval setting. Final images were deconvoluted using NIS analysis software.

For resonant scanning mode imaging during FRAP assays, after choosing Resonant mode on the NIKON A1 microscope, a ×100 objective was used to collect images at 512 × 512 pixels, 7 frames s<sup>-1</sup>, no-delay setting. Final images were deconvoluted using NIS analysis software.

**Photoconversion experiments.** All the photoconversion experiments were conducted using a NIKON A1 confocal microscope in resonant scanning mode, fitted with a ×100 oil objective and three times zoom in. The area of interest area was photoconverted by 405 nm laser with 10% output for 1 s. Immediately after conversion, 488 nm and 561 nm lasers were applied for imaging, and each field of 512 × 512 pixels was imaged for 3 min.

**LPDS treatment.** LPDS was prepared from fetal bovine serum (FBS) as previously described<sup>28,29</sup>. To promote cellular cholesterol depletion, TSPAN4-GFP-expressing NRK cells were cultured in DMEM supplemented with 10% FBS, LPDS or LPDS with 30 µM pravastatin (TargetMol, T0672) for 48 h. Then, the cells were digested using trypsin and transferred to fibronectin-coated glass-bottom dishes containing the respective medium for another 12 h. Following treatment for 60 h, live-cell images were randomly acquired to analyse migrasome numbers, and the total cellular cholesterol levels of each group were determined using an Amplex Red cholesterol assay kit (Invitrogen, A12216) according to the manufacturer’s instructions.

**Quantitative real-time PCR.** MGC-803 cells were cultured on fibronectin-coated dishes for 12 h to reach 60–70% confluence. Total RNA was isolated using TRIzol reagent (Invitrogen, 15596026). cDNA was synthesized using a ReverTra Ace qPCR RT kit (TOYOBO, FSQ-101) with a primer mix (Random primer + Oligo (dT) primer). Quantitative real-time PCR was performed in triplicate using 2× T5 Fast qPCR Mix (SYBR Green I) (TSINGKE Biological Technology, TSE202) on a LightCycler 480 Instrument II (Roche Life Science). Primers for the following genes were identified from the MGH PrimerBank<sup>30–33</sup>: TSPAN1 (ID: 274317624c1), TSPAN2 (ID: 269995931c1), TSPAN4 (ID: 68800031c1), TSPAN6 (ID: 21265115c1), TSPAN7 (ID: 183396766c2), TSPAN9 (ID: 270132568c1), TSPAN18 (ID: 283135198c1), CD81 (ID: 6224099c1), CD82 (ID: 67782353c2) and GAPDH (ID: 378404907c1). Relative mRNA levels of TSPAN genes were normalized to TSPAN4 and analysed using the 2–ΔΔCt method. The final statistics and generation of graphs were conducted using Graphpad Prism 7.0.

**AFM-based liposome-bending rigidity measurement.** Proteoliposomes with different concentrations of cholesterol (0, 10, 20 and 30%) and TSPAN4-GFP protein (0, 0.1 and 0.2 mg ml<sup>-1</sup>) were prepared as described above, except that the filter size was changed from 1,000 nm to 200 nm. Then the proteoliposomes were applied to the glass slides, which were pretreated with PEG-biotin and then coated with streptavidin (1 mg ml<sup>-1</sup>). After washing in HEPES buffer II (10 mM HEPES, pH 7.4, 150 mM NaCl), the sample was applied to the AFM force-measuring setting. By using the constant force mode, more than 1,000 force-to-distance traces were collected and more than 500 traces were selected for each sample. After linear fitting calculation, the first stage slope  $K_1$  (pN nm<sup>-1</sup>) of each trace was measured. Finally, the mean  $K_1$  of a group of proteoliposomes was calculated by Gaussian fitting. At the same time, the mean radius (nm) of each group of proteoliposomes was measured by dynamic light scattering followed by Gaussian fitting. The final bending rigidity of each kind of proteoliposome was calculated as a function of  $K_1$  and the radius.

**Single-molecule counting by PALM.** NRK cells transfected with TSPAN4-mMaple3 were grown on fibronectin-coated chambers for 15 h. The cells were fixed using paraformaldehyde, then examined under 3D-PALM. The software Insight3 developed by X. Zhuang's Lab was used to analyse the original images from PALM to calculate and determine the position of single TSPAN4 molecules, which were represented by coloured points. The colour ranges from red to blue indicate the z-positions from the bottom to the top of the imaging section. The area ranges were precisely set to encompass our regions of interest (ROIs), including the migrasomes and RFs, and the number of single TSPAN4 molecules in these ROIs was counted. By estimating migrasomes and RFs as spheres and cylinders, respectively, the surface area of the ROIs could be measured and calculated. Finally, the number of TSPAN4 molecules per unit of surface area on migrasomes and RFs was estimated by calculation.

**Estimate of the enrichment of cholesterol relative to TSPAN4-GFP on migrasomes.** NRK cells with stable TSPAN4-GFP expression were cultured on fibronectin-precoated confocal dishes for 15 h, then treated with 2 µg ml<sup>-1</sup> filipin III (which specifically stains cholesterol) for 15 min at 37 °C. Z-stack images were acquired by confocal microscopy with a z-step of 200 nm to visualize the migrasomes and RFs. After two-dimensional projection of the total fluorescence signals, ImageJ was used to measure the filipin III intensity on migrasomes (IpM), the TSPAN4-GFP intensity on migrasomes (ItM), the filipin III intensity on RFs (IpR) and the TSPAN4-GFP intensity on RFs (ItR). A migrasome and its connected length of RF were set as a pair. Within a pair, the value of IpM/IpR and the value of ItM/ItR were calculated. Then, the fold-change of filipin III intensity on migrasomes relative to RFs, IpM/IpR, was normalized by the fold-change of TSPAN4-GFP intensity on migrasomes relative to RFs, ItM/ItR.

**Statistics and reproducibility.** All experiments were conducted independently at least three times, except for experiments related to Fig. 1a and Supplementary Table 1, which were done once. Experiments for quantification of migrasome numbers and migrasome numbers per unit of RF length in vivo and in vitro were performed three times. Experiments including FRAP and photoconversion experiments were performed at least five times. Experiments related to membrane-bending rigidity measurement were performed three times. For quantification of migrasomes, at least 80 random cells were chosen and the numbers of migrasomes were counted.

To calculate migrasome numbers per unit of RF length in vivo, the total number of migrasomes was counted and the total length of RFs was measured in more than 50 randomly selected cells. To calculate migrasome numbers per unit of tether length in vitro, the length of each tether was measured and the total number of migrasomes on the tether was counted for more than 89 randomly selected tethers. For cluster density statistics, 12 experiments were conducted, and more than 12 RFs and 38 migrasomes were analysed. For single-molecule counting assays, 9 sets of data were collected, and 30 pairs of migrasomes and RFs were analysed. For analysis of the fluorescence intensity of migrasome and RFs in vivo, more than 255 pairs of migrasomes and RFs were randomly analysed. Statistical analyses were conducted using the unpaired two-tailed *t*-test in Graphpad Prism 5. Error bars are the mean ± s.e.m. \**P* < 0.05, \*\**P* < 0.01, \*\*\**P* < 0.001, NS, not significant.

**Reporting Summary.** Further information on research design is available in the Nature Research Reporting Summary linked to this article.

## Data availability

Statistical source data for Figs. 1–5, Supplementary Figs. 1 and 3 and Supplementary Tables 2 and 3 have been provided as Supplementary Table 4.

## Code availability

The main computational codes used for the simulations in this paper are available at <https://github.com/benzucker-tau/Migrasome-simulation>. Further codes in surface evolver and codes in Matlab used for analyses are available from the corresponding authors upon reasonable request.

## References

25. Su, Q. P. et al. Vesicle size regulates nanotube formation in the cell. *Sci. Rep.* **6**, 24002 (2016).
26. Du, W. et al. Kinesin 1 drives autolysosome tubulation. *Dev. Cell* **37**, 326–336 (2016).
27. Wang, C. et al. Dynamic tubulation of mitochondria drives mitochondrial network formation. *Cell Res.* **25**, 1108–1120 (2015).
28. Martin, B. J. & van Golen, K. L. A comparison of cholesterol uptake and storage in inflammatory and noninflammatory breast cancer cells. *Int. J. Breast Cancer* **2012**, 412581 (2012).
29. Renaud, J. F. et al. Normal serum and lipoprotein-deficient serum give different expressions of excitability, corresponding to different stages of differentiation, in chicken cardiac cells in culture. *Proc. Natl Acad. Sci. USA* **79**, 7768–7772 (1982).
30. Wang, X. & Seed, B. A PCR primer bank for quantitative gene expression analysis. *Nucleic Acids Res.* **31**, e154 (2003).
31. Spandidos, A. et al. A comprehensive collection of experimentally validated primers for polymerase chain reaction quantitation of murine transcript abundance. *BMC Genomics* **9**, 633 (2008).
32. Spandidos, A., Wang, X., Wang, H. & Seed, B. Primer bank: a resource of human and mouse PCR primer pairs for gene expression detection and quantification. *Nucleic Acids Res.* **38**, D792–D799 (2010).
33. Wang, X., Spandidos, A., Wang, H. & Seed, B. PrimerBank: a PCR primer database for quantitative gene expression analysis, 2012 update. *Nucleic Acids Res.* **40**, D1144–D1149 (2012).

# Reporting Summary

Nature Research wishes to improve the reproducibility of the work that we publish. This form provides structure for consistency and transparency in reporting. For further information on Nature Research policies, see [Authors & Referees](#) and the [Editorial Policy Checklist](#).

## Statistics

For all statistical analyses, confirm that the following items are present in the figure legend, table legend, main text, or Methods section.

n/a Confirmed

- The exact sample size ( $n$ ) for each experimental group/condition, given as a discrete number and unit of measurement
- A statement on whether measurements were taken from distinct samples or whether the same sample was measured repeatedly
- The statistical test(s) used AND whether they are one- or two-sided  
*Only common tests should be described solely by name; describe more complex techniques in the Methods section.*
- A description of all covariates tested
- A description of any assumptions or corrections, such as tests of normality and adjustment for multiple comparisons
- A full description of the statistical parameters including central tendency (e.g. means) or other basic estimates (e.g. regression coefficient) AND variation (e.g. standard deviation) or associated estimates of uncertainty (e.g. confidence intervals)
- For null hypothesis testing, the test statistic (e.g.  $F$ ,  $t$ ,  $r$ ) with confidence intervals, effect sizes, degrees of freedom and  $P$  value noted  
*Give  $P$  values as exact values whenever suitable.*
- For Bayesian analysis, information on the choice of priors and Markov chain Monte Carlo settings
- For hierarchical and complex designs, identification of the appropriate level for tests and full reporting of outcomes
- Estimates of effect sizes (e.g. Cohen's  $d$ , Pearson's  $r$ ), indicating how they were calculated

*Our web collection on [statistics for biologists](#) contains articles on many of the points above.*

## Software and code

Policy information about [availability of computer code](#)

### Data collection

Images were collected by FV1200 and FV1000 (Olympus), movies and FRAP assays were conducted by NIS-Elements AR-4.3 (Nikon), Bending rigidity measurement and calculation based on data collected by Atomic force microscope (set up by Jizhong Lou Laboratory, Institute of Biophysics, Chinese Academy of Sciences) and DynaPro NanoStar for dynamic light scattering measuring (Wyatt).

### Data analysis

**Software:**  
 Image J was used for 1. measurement and analysis the amounts and lengths of in-vitro system migrasomes and retraction fibers. 2. Fluorescence intensity and gray value of images.  
 GraphPad Prism 5 was used for statistic analysis.  
 Graphpad Prism7.0 was used for statistics analysis and graph making related to mRNA levels and cholesterol levels verification.  
 Imaris 9.0.2 was used for reconstitution movie analysis and signals tracing.  
 NIS-elements-AR4.30.02 was used for fluorescent intensity and area analysis in movies.  
 Adobe Illustrator CC 2015 was used for images composing and exhibition.  
 The Surface Evolver Version 2.70 was used for modeling parts.  
 Origin9.2 was used for Gaussian fitting analysis.  
 Instight3 4.22.2(designed by Xiaowei Zhuang's Lab) was used for 3D-PALM single molecule counting.  
**Code:**  
 The main computational codes used for the simulations in this paper are available at <https://github.com/benzucker-tau/Migrosome-simulation>. Further codes in surface evolver and codes in Matlab used for analyses are available from the corresponding authors upon request.

For manuscripts utilizing custom algorithms or software that are central to the research but not yet described in published literature, software must be made available to editors/reviewers. We strongly encourage code deposition in a community repository (e.g. GitHub). See the Nature Research [guidelines for submitting code & software](#) for further information.

## Data

Policy information about [availability of data](#)

All manuscripts must include a [data availability statement](#). This statement should provide the following information, where applicable:

- Accession codes, unique identifiers, or web links for publicly available datasets
- A list of figures that have associated raw data
- A description of any restrictions on data availability

Statistical Source Data for Fig.1-Fig.5, Supplementary Fig.1, Supplementary Fig. 3 and Supplementary Table 2- Table 3 have been provided as Supplementary Table 4. All other data that support the findings of this study are available from the corresponding author upon request.

## Field-specific reporting

Please select the one below that is the best fit for your research. If you are not sure, read the appropriate sections before making your selection.

Life sciences       Behavioural & social sciences       Ecological, evolutionary & environmental sciences

For a reference copy of the document with all sections, see [nature.com/documents/nr-reporting-summary-flat.pdf](https://nature.com/documents/nr-reporting-summary-flat.pdf)

## Life sciences study design

All studies must disclose on these points even when the disclosure is negative.

Sample size	No statistical methods were used to determine sample size. For all the experiments, we followed the routine practice in the similar studying fields. And it has been our routine practice to conduct experiments upon a relatively large but reasonable size.
Data exclusions	No data were excluded from the analysis.
Replication	Attempts at replication were successful. For all experiments, except experiments related to Fig.1a and Supplementary Table 1 (which were done once. ), at least 3 times independent experiments were repeated with the similar results as presented in this study. Detail information was involved in the Methods--Statistics and reproducibility section, as well as Statistics Source Data.
Randomization	Microscopic images were acquired randomly.
Blinding	The investigators were not blinded to allocation during experiments and outcome assessment. Within each experiment, at least one negative control group was set to ensure that only one variate was tested. And because all the data were conducted based on random sampling and reasonably large sample size, blinding is not relevant to this study.

## Reporting for specific materials, systems and methods

We require information from authors about some types of materials, experimental systems and methods used in many studies. Here, indicate whether each material, system or method listed is relevant to your study. If you are not sure if a list item applies to your research, read the appropriate section before selecting a response.

### Materials & experimental systems

n/a	Involved in the study
<input type="checkbox"/>	<input checked="" type="checkbox"/> Antibodies
<input type="checkbox"/>	<input checked="" type="checkbox"/> Eukaryotic cell lines
<input checked="" type="checkbox"/>	<input type="checkbox"/> Palaeontology
<input checked="" type="checkbox"/>	<input type="checkbox"/> Animals and other organisms
<input checked="" type="checkbox"/>	<input type="checkbox"/> Human research participants
<input checked="" type="checkbox"/>	<input type="checkbox"/> Clinical data

### Methods

n/a	Involved in the study
<input type="checkbox"/>	<input checked="" type="checkbox"/> ChIP-seq
<input checked="" type="checkbox"/>	<input type="checkbox"/> Flow cytometry
<input checked="" type="checkbox"/>	<input type="checkbox"/> MRI-based neuroimaging

## Antibodies

### Antibodies used

Anti-GFP antibody (MBL), Cat# 5985, RRID:AB\_591816, 1:1000 dilution  
 Anti-beta-Actin Mouse mAb (Zen-bioscience), Cat# 200068-8F10, RRID: AB\_2722710, 1:1000 dilution  
 Anti-GAPDH antibody (proteinintech), Cat# 60004-1-Ig, RRID: AB\_2107436, 1:1000 dilution  
 Goat-Anti-Mouse IgG-HRP (Southern Biotech), Cat# 1010-05, RRID: AB\_2728714, 1:5000 dilution  
 Goat-Anti-Rabbit IgG-HRP (Southern Biotech), Cat# 4010-05, RRID: AB\_2632593 1:5000 dilution

### Validation

All the antibodies were validated by western blot.  
 Anti-GFP antibody was validated by the manufacturer using western blot. Species reactivity: Bovine, Canine, Chicken/avian, Donkey, Drosophila, Feline, Guinea pig, Hamster, Human, Mouse, Porcine, Rabbit, Rat, Sheep, Simian, Xenopus, Yeast.

Anti-beta-Actin was validated by the manufacturer using western blot. Species reactivity: Human, Mouse, Monkey, Goat, Rat, Hamster, *Saccharomyces cerevisiae*, *Arabidopsis*, *Pichia pastoris*, Rabbit, Zebrafish, *Drosophila*, Leaf of Rice, Fruit of Cucumber, *Chlamydomonas Reinhardtii*, Fish, Pig, Chicken.

Anti-GAPDH was validated by the manufacturer using western blot. Species reactivity: human, mouse, rat, zebrafish, yeast, plant, beagle, carp, chicken, cow, *Cynomorium songaricum* Rupr, *Cyprinus carpio*, deer, dog, Eelworm, *H. illucens*.

Goat-Anti-Mouse Ig Human ads-HRP were validated by the manufacturer using western blot. Specificity: Reacts with the heavy and light chains of mouse IgG1, IgG2a, IgG2b, IgG2c, IgG3, IgM, and IgA.

Goat-Anti-Rabbit Ig Human ads-HRP were validated by the manufacturer using western blot. Specificity: Reacts with the heavy and light chains of rabbit IgG and IgM.

## Eukaryotic cell lines

Policy information about [cell lines](#)

Cell line source(s)

NRK (ATCC), CRL-6509™  
Human MGC803, gift from Zhijie Chang laboratory, Tsinghua University  
Mouse L929 (ATCC), CCL-1  
293F, gift from Laboratory of Yigong Shi, Tsinghua University

Authentication

The cell lines were not authenticated.

Mycoplasma contamination

The cell lines were not tested for mycoplasma contamination.

Commonly misidentified lines  
(See [ICLAC](#) register)

No cell lines used in this study were found in the database of commonly misidentified cell lines that is maintained by ICLAC and NCBI Biosample.